

Study on local shear mechanism in direct shear test of rough rock joints based on DEM

Jiuyang Huan

Yangzhou Polytechnic Institute

Zhiqiang Zhang (✉ 2668709921@qq.com)

Xi'an University of Technology

Mingming He

Xi'an University of Technology

Ning Li

Xi'an University of Technology

Mengdie Hu

Yangzhou Polytechnic Institute

Article

Keywords: JRC, Local shear mechanism, Joint segment, protrusion size, Shear stress, DEM

Posted Date: March 17th, 2022

DOI: <https://doi.org/10.21203/rs.3.rs-1449547/v1>

License:   This work is licensed under a Creative Commons Attribution 4.0 International License.

[Read Full License](#)

Abstract

Rough joints widely exist in natural rock mass, and their shear mechanical properties control the safety and stability of rock mass. In the existing studies, the contribution of different protrusions to resisting shear stress is not mentioned. In this study, the local shear mechanism of different protrusions of rough joints in the shear process were well presented by combining quantitative and qualitative results using the discrete element method (DEM). Firstly, Barton's 10 standard roughness joint profiles were digitized. Rough joints were established using the modified smooth joint model (MSJM). The direct shear tests of joint specimens under constant normal stress were successfully conducted based on servo mode. Secondly, according to the test results, the law of shear stress was discussed. Then, the failure mode of joint specimen was discussed in detail based on the crack tracking module and force chain analysis. Next, the relationship between the number of cracks and shear stress was investigated. Finally, the variation law of average stress in different 10 segments of joints during shear was tracked based on the measuring circle function. The contribution of local joint segments in resisting shear stress is quantitatively described by 3 stress indexes.

1. Introduction

Rough joints widely exist in natural rock mass and have different morphologies, scales and directions¹⁻³. The characteristics of multiple fractures make the rock mass have typical characteristics such as discontinuity, heterogeneity and anisotropy, which is obviously different from the complete rock block⁴⁻⁶. The overall stability of rock mass can be evaluated by deformation law and failure characteristics. A large number of engineering practices showed that the joint surface in rock mass plays a leading role in the deformation and failure of rock slope and tunnel surrounding rock⁷⁻⁸. This is because the failure of rock mass usually occurs first along the joint surface, and then produces a series of chain failure reactions, which eventually leads to the large-scale failure of the whole rock mass. Therefore, accurately understanding the mechanical properties of structural plane is an important basis for evaluating the stability and safety of engineering rock mass⁹⁻¹¹.

Traditionally, the shear mechanical properties of rock joints were studied by using natural joint surfaces. The joint surface was first taken out from the rock mass and made into a sample, and then a shear test was carried out. In most cases, each joint surface can only undergo one shear process under the same conditions. In other cases, the joint surface will undergo multiple shear process to explore the weakening law of shear stress and rough morphology^{12,13}. Since the natural joint surface will have some failure after one shear failure, so it is inconvenient to systematically carry out the influence of different influencing factors such as normal stress and roughness on the shear characteristics of the joint.

In order to solve the above problem, researchers used other materials to simulate rock to study the shear mechanical properties of joints, such as mortar and gypsum samples¹⁴⁻¹⁶. In these physical tests, the joint surface was been set to different roughness through the mold, including regular and irregular types. The joint samples with the same morphology could be infinitely copied by rock like materials, this is

conducive to the setting of different research schemes of direct shear test. After that, the shear mechanical properties (such as shear stress, normal deformation, failure scale, etc) of rock joints under different boundary conditions, roughness, shear velocity, filling degree, rock mass type and other influencing factors were continuously revealed¹⁷⁻¹⁹. However, it is worth noting that the above studies are carried out on the basis of indoor physical experiments. Researchers can only observe the failure of the sample after the shear process, but cannot clearly understand the failure mechanism of the geometric morphology of the joint during the shear process.

In recent decades, the application of numerical simulation technology in the field of geotechnical engineering was expanding day by day^{20,21}. With the continuous updating of computer software and hardware, the discrete element method (DEM) that was derived from particulate and blocky theory systems had a rapid development^{22,23}. The potential advantage of the DEM is that the mechanical response of jointed rock mass can be derived based on simple particle contact logic. In the numerical test based on DEM, the test boundary and parameters can be simply set, and the test results can be easily monitored^{24,25}. For the direct shear test of numerical joint samples, the key is that the failure law of samples in the shear process can be well presented. At present, many scholars had carried out many useful studies on the shear mechanical properties of joint samples based on DEM and achieved rich research results²⁴⁻²⁸.

As one of the important factors affecting the shear mechanical properties of rock joints, the roughness of rock joints had been widely concerned by researchers in recent decades. Since Barton proposed using joint roughness JRC to quantitatively describe the roughness of joints, many scholars had established the functional relationship between JRC and different morphological parameters such as the root mean square of the first deviation of profiles (Z_2) and the roughness profile index (R_p-1)^{29,30}. However, in the calculation formulas of most morphological parameters, all fluctuations on the joint surface were calculated, and the idea of averaging was adopted. Obviously, this process ignored the differences of failure mechanisms of protrusions with different sizes, which was obviously unreasonable. The reason is that the quantitative results of the difference of local fluctuation in resisting shear stress were rarely mentioned in the existing joint direct shear test research.

To compensate for this shortcoming, this paper will present the local shear mechanism of different protrusions of rough joints in the shear process by combining quantitative and qualitative results. Numerical rock specimens containing rough joints were established using the particle flow software (PFC^{2D}) in discrete element method (DEM). The Barton's 10 standard roughness joint were simulated using the modified smooth joint model (MSJM)²⁵⁻²⁶ and the direct shear tests of these joint specimens under constant normal stress were successfully carried out based on servo mode.

Based on the test results, the law of shear stress was discussed firstly. Based on the crack tracking module, the failure mode of joint specimen was discussed in detail, and the relationship between the number of cracks and shear stress was also presented. Based on the built-in measuring circle function of

PFC^{2D}, the variation law of average stress in different segments of joints during shear was tracked. The contribution of local joint segments in resisting shear stress was related to the geometric morphology of joints and quantitatively described by several stress indexes. Finally, the local shear mechanism of joints is well presented and provides an important reference for subsequent research.

2. Acquisition Of Rough Joint Profile

2.1 Digitization of Barton's 10 joint profiles

In 1978, Barton first proposed 10 standard roughness joint profiles in an article and gave the JRC inverse value of these joints when they are sheared from left to right. This work provided an important way for the quantitative description of rock joint roughness³¹⁻³³. After that, many researchers studied the shear mechanical properties and roughness description methods of rock joints based on the above typical joint profiles³⁴⁻³⁶. Due to the lack of original data, subsequent researchers usually obtained the geometric coordinates of 10 joint profiles through various indirect methods.

The original data of 10 joint profiles were obtained by Barton^{31,32} through the profile comb, and the sampling interval was 0.5mm (Fig. 1). In this study, an image recognition method was used to digitize the joint profiles, which was close to the re-acquisition of the original data. The image processing software was chosen to be GETDATA. In order to avoid data distortion, the digitization process of joint profiles in this paper also maintained the same sampling interval.

2.2 Validation of joint profile data

In order to verify the reliability of the digitization process of the 10 joint profiles in section 2.1, statistical parameters Z_2 and R_p-1 which are widely used to describe joint roughness in geotechnical engineering were recommend as representative for verification. Their definitions are as follows²⁹⁻³⁰:

$$Z_2 = \left[\frac{1}{L} \int_{x=0}^{x=L} \left(\frac{dy}{dx} \right)^2 dx \right]^{1/2} = \left[\frac{1}{(N-1)(\Delta x)^2} \sum_{i=1}^{N-1} (y_{i+1} - y_i)^2 \right]^{1/2} \quad (1)$$

$$R_p-1 = \frac{\sum_{i=1}^{N-1} [(x_{i+1} - x_i)^2 + (y_{i+1} - y_i)^2]^{1/2}}{L} - 1 \quad (2)$$

Where N is the number of discrete points in joint profile and it is 201 at 0.5 mm sampling interval. At 0.5mm sampling interval, the values of Z_2 and R_p-1 of 10 standard roughness joint profiles were calculated by Eq. (1) and Eq. (2). Eq. (3) was selected to establish fitting relationship between statistical parameters and JRC.

$$JRC = a \cdot \ln(P) + b \quad (3)$$

Where P represents the statistical parameters, a and b is the regression coefficients. As showed in Fig. 4, with the increase of JRC, the values of Z_2 and $RP-1$ showed an increasing trend as a whole. The

correlation coefficients squared (R^2) of Z_2 and R_{p-1} with JRC calculated in our paper all exceeded 0.95, which was basically consistent with the findings of other researchers³⁴⁻³⁵. This confirmed that the data acquisition work of the 10 standard joint profiles in our paper was very accurate. On this basis, follow-up studies were reliable.

3. Direct Shear Test Of Joint Specimens

The numerical model and direct shear test of joint specimens were simulated by the Particle Flow Code software (PFC^{2D}). In this software, the mechanical behavior of materials could be simulated by displacement and force interaction in particles. The basic relationship between forces and motion of particles is Newton's second law of motion³⁷.

3.1 Establishment of numerical model

In earlier numerical studies, many scholars used bond removal method (BRM) to generate joint²²⁻²³. Since joint can only occur at the contact of particles, the roughness of joint generated by the BRM is greatly affected by particle distribution. Later, the smooth joint model (SJM) was introduced into PFC and allows particles to pass through or overlap each other rather than to spin around each other. So, the SJM solved the shortcomings of the BRM very well and had been widely used in numerical studies of jointed rock masses²⁴⁻²⁶. However, Bahaaddini et al.²⁶ found that the smooth joint model might lead to an unreliable increase in the shear strength and normal displacement of joint sample. Finally, the modified smooth joint model (MSJM) had been proposed to achieve better simulation results. In this paper, the same idea was used to establish the numerical model of joint specimens.

Firstly, two contact boxes were established and each box had four frictionless walls. The overall dimensions of the model were 100 mm in width and 60 mm in height. The upper wall of the box below and the bottom wall of the upper box were overlapping. They were generated from the geometric coordinates of the 10 standard roughness joint profiles obtained in Section 2.1. The input of the joint node must follow the right-hand rule as only one face of the wall is active by default.

Second, randomly placed particles were separately generated in the upper and lower parts of the joint sample. The particle size is between 0.15 mm and 0.24mm, which satisfied uniform size distribution. Each numerical joint specimens contained 41 883 particles at a porosity of 0.15. At the beginning of particle formation, there was many overlaps between the particles. After giving an initial stiffness, the overlapping particles generated previously were allowed to rearrange and reached the static equilibrium under friction free conditions. Next, particles with less than one contact were eliminated to reduce internal locking phenomenon²⁴⁻²⁶.

Then, the BPM was installed on the upper and lower parts of the specimen respectively and the two rough walls in the middle of the specimen were deleted. Next, an appropriately low normal pressure was applied to the specimen. New contacts were generated between the particles of the upper and lower part of

the specimen. Finally, the discrete fractures network (DFN) was applied to determine the location of 10 rough joint profiles, and the SJM was applied at the DFN³⁷. According to the above ideas, joint samples with 10 standard roughness were established respectively. Figure 5 shows the 7th joint specimen for illustration.

3.2 Setting and calibration of microscopic parameters

In DEM such as PFC^{2D}, the macroscopic mechanical behavior of the material that we are expecting to simulate is derived by the interaction of constituents such as particle and bond. So far, researchers had not found that the micro parameters of these components have a specific corresponding relationship with the macroscopic mechanical behavior of the model. Therefore, these microscopic parameters must be calibrated through repeated trial and error of conventional physical tests.

3.2.1 Calibration process of microscopic parameters of the BPM

In order to calibrate microscopic parameters of the BPM applied in intact rock, numerical specimen with length of 50 mm and height of 100 mm were generated²²⁻²⁸. The setting of particle distribution and microscopic parameters is completely consistent with Section 3.2. The specimen contained 34901 particles. The uniaxial compression tests were carried out without confining pressure, and the result showed that the uniaxial compressive strength (UCS) was 59.09 MPa and the deformation modulus (E_0) was 8.83 GPa for the intact rock. The macroscopic mechanical properties and failure mode of the numerical specimen were consistent with the physical test results of real rock (Fig. 6). The calibrated microscopic parameters of BPM are summarized in Table 1.

Table 1. Microscopic parameters of balls and bonds in intact rock.

Particle parameters		Parallel bond parameters	
Particle density [kg/m ³]	2000	Modulus E^* [GPa]	5.5
Modulus E^* [GPa]	5.5	Stiffness ratio k_n/k_s	1.5
Stiffness ratio k_n/k_s	1.5	Tensile strength [MPa]	34.5
Friction coefficient μ	0.7	Cohesion [MPa]	34.5

3.2.2 Calibration process of microscopic parameters of the SJM

In order to calibrate microscopic parameters of the SJM, the direct shear tests on planar joints were conducted. The establishment of joint specimen is consistent with Section 3.1, while the position of rough joints is replaced with a flat joint established by the SJM. In the direct shear tests, a constant normal stress was applied to the top wall by using a servo mechanism (see section 3.4 for details). The shear stress shear displacement curves of numerical direct shear test of flat joints under normal stresses

of 2, 4, 6 and 8MPa are shown in Fig. 7. It can be seen that the shear stress curve shows the characteristics of slip failure, which is consistent with the indoor physical test.

As shown in Fig. 7(b), the difference of shear strength results between numerical test and indoor physical test of flat joints under the same scheme was very small and the friction angle of joint surface was near 40.22°. Therefore, it can be considered that the simulation and parameter setting of joint surfaces in the numerical calculation of this paper are very reasonable. The calibrated microscopic parameters of the SJM were presented in Table 2.

Table 2. Microscopic parameters of joint surface.

Normal stiffness	Shear stiffness	Friction coefficient	Large deformation
sj_{kn}	sj_{ks}	sj_{fric}	sj_{large}
[GPa/m]	[GPa/m]		
400	100	0.83	1

3.3 Shearing process control

Figure 8 shows the scheme of the direct shear test of rough joint specimen. 3#, 4# and 5# walls belong to the upper shear box and 1#, 2# and 6# walls belong to the lower shear box. During the direct shear test, the lower shear box was fixed and a constant horizontal velocity of 4 mm/s was applied to the upper shear box. Shear stress and shear strain could be calculated by recording the force and displacement of the corresponding wall including 2#, 5# and 6# walls.

The calculations in PFC software were carried out by a time-stepping algorithm. The real time between each calculation step had a small value about 2.904×10^{-7} s. That is, the upper and lower wall moved at the rate of 11.616×10^{-7} mm per time step. This movement rate was so slow enough to ensure that the test process of joint specimen was in quasi-static equilibrium. The direct shear tests of joint specimens with 10 standard roughness were carried out and the shearing direction was from left to right by default.

3.4 Servo mechanism

During the direct shear test under constant stress conditions, the normal stress applied to the upper and lower surfaces of sample must be kept constant. However, the direct application of load cannot be realized in the PFC software. The constant load state could only be maintained by a servo function that can automatically changing the normal moving speed of the upper and lower walls at each calculation step.

The normal velocity $v^{(wall)}$ of the upper surface of joint specimen could be set as follows:

$$v^{(wall)} = G(\sigma^{\text{measure}} - \sigma^{\text{require}}) = G\Delta\sigma \quad (4)$$

Where G represent the servo parameter, $\sigma^{measure}$ represented the normal stress actually applied to the upper surface of the joint specimen, $\sigma^{require}$ represented the expected normal stress set by us and $\Delta\sigma$ represent the stress difference between $\sigma^{measure}$ and $\sigma^{require}$. The maximum value of $\Delta\sigma$ was defined as:

$$\Delta\sigma^{(wall)} = (k_n^{(wall)} N_c v^{(wall)} \Delta t) / A \quad (5)$$

In Eq. (5), $k_n^{(wall)}$ represented the average stiffness of the particles in contact with 1# and 4# walls, N_c represent the number of particles and A represent the area of the wall. In order to minimize the difference between $\sigma^{measure}$ and $\sigma^{require}$, a release factor α was introduced as shown in Eq. (6).

$$|\Delta\sigma^{(wall)}| < \alpha |\Delta\sigma| \quad (6)$$

When substituting Eq. (4) and Eq. (5) into Eq. (6), the Eq. (7) could be obtained.

$$(k_n^{(wall)} N_c G |\Delta\sigma| \Delta t) / A < \alpha |\Delta\sigma| \quad (7)$$

Thus, the servo coefficient G could be defined as follows:

$$G = \alpha A / (k_n^{(wall)} N_c \Delta t) \quad (8)$$

When the software runs a calculation step, the servo parameter G of the next calculation step is calculated by the servo function in advance. The normal velocity $v^{(wall)}$ of the upper walls will be updated by Eq. (4). Next, the servo parameter G required for the next calculation step is also calculated simultaneously.

In order to verify the reliability of the above method, the direct shear tests of planar joint under normal stress conditions of 1MPa, 2MPa and 3MPa were carried out. After data monitoring, Figure 9 shows the normal stresses applied to the upper and lower walls. It could be seen that $\sigma^{measure}$ and $\sigma^{require}$ was very close and the normal stress application process was very stable and reliable. In the follow-up study, the normal stresses applied to the joint specimens were 2 MPa, 4 MPa, 6MPa and 8 MPa respectively.

4. Test Results

4.1 Shear stress curve and shear strength

Based on the direct shear test, the results of shear stress shear displacement curves of joint samples with different roughness are given in Fig. 10. Here, only the condition of normal stress 2MPa and 6MPa were taken as a representative for discussion.

It can be seen from the figure that the shear stress curve was roughly divided into two stages. At the beginning of the shear process, the shear stress increased very rapidly, and the joint roughness had little effect on the growth rate of shear stress. With the continuous increase of shear displacement, the growth rate of shear stress decreased gradually, and then reached the peak value. The above process was

defined as the pre peak stage. With the increase of joint roughness, the growth rate of shear stress in the pre peak stage increased faster. After that, the shear stress curve entered the post peak stage. The shear stress decreased greatly firstly, and finally remained basically constant in a certain range. As the joint roughness and normal stress increased, the reduction effect of shear stress curve in the post peak stage was more obvious.

Figure 11(a) shows the relationship curve between joint JRC and shear strength under different normal stress conditions. It can be seen that the shear strength shows an obvious increasing trend with the increase of joint JRC. This indicates that the numerical shear test can well reflect the influence of joint JRC on joint shear strength.

Figure 11(b) shows the relationship between normal stress and shear strength under different joint roughness. It can be seen that the shear strength increases approximately linearly with the increase of normal stress, and the rules of joints with different roughness are very similar.

4.2 Failure mode of joint specimen

In the numerical rock specimens established by PFC^{2D}, when the stress acting between particles is greater than the parallel bond parameters summarized in Table 1, the contact will be damaged and cracks will occur. The microcracks produced in the shear process of rock specimens can be tracked by writing a specific command flow³⁷.

In order to show the failure mechanism of joint samples during shear, Contrast diagram of crack propagation and contact force distribution of joint specimen under different shear displacements are given in Fig. 12. Among them, the 10th joint specimen under normal stress of 4MPa is selected for description, and the shear displacement is 0mm, 0.5mm, 0.75mm, 1mm, 2mm and 3mm respectively. In the crack propagation diagram, the blue part is the upper sample, the green part is the lower sample, the red represents the crack, and the white area at the joint surface is the gap. In the contact force distribution diagram, black represents the contact force chain. The darker and thicker the color of the force chain, the greater the contact force.

Before the start of shearing (Fig.12(a)), there was no crack in the sample, and the internal contact force was evenly distributed. When the shear displacement was 0.5mm (Fig.12(b)), there were a few cracks on the large protrusion of the joint surface and the contact force had shown a concentration effect. The contact force at the protrusion where the crack is concentrated was relatively large. When the shear displacement was 0.75mm (Figure12(c)), the number of cracks on larger protrusions had increased and gradually deepened. In addition, some small protrusions were also damaged at this time. On the whole, the contact force concentration effect of joint specimens had been very obvious at three large protrusions.

When the shear displacement was 1mm (Fig.12(d)), the maximum protrusion of the sample was damaged, which led to the rapid increase of the number of cracks in the specimen. In addition, the

increase of shear displacement caused the dislocation of joint surface and the concentration range of contact force decreased. When the shear displacement increased from 1mm to 2mm (Fig.12(d) to (e)), the contact force concentration effect at the maximum protrusion decreased significantly. At this time, the contact force of the middle protrusion was the largest, which led to its partial failure. When the shear displacement increased from 2mm to 3mm (Fig.12(e) to (f)), new contact occurred on the joint surface due to dislocation. These new contacts continued to resist shear stress and subsequently failed.

We can realize that the large protrusions of the joint surface made a great contribution to the resistance to shear force. It not only had a large failure scale, but also the failure time was very early. In contrast, the contribution of small protrusions in resisting shear force was relatively small. They only had a small amount of damage or even no damage, and the time point of damage was later. It can be seen that the joint surface showed a progressive failure mechanism, and the size of protrusion in joint surface had an important influence on the resistance to shear stress.

4.3 Relationship between crack number and shear stress

During the shear process, the joint protrusion resisted the shear stress by squeezing each other. Only a large shear force could make the joint protrusion produce cracks and damage, so there must be a relationship between the development of shear stress and crack propagation. Figure 13 shows change curves of shear stress and crack number with shear displacement under 4MPa normal stress for the typical description. Figure 13(a) to (d) show the 1th joint, the 4th joint, the 7th joint and the 10th joint respectively.

In the initial stage of shear process, the shear stress increased fastest, but there was no crack in the sample. With the gradual increase of shear displacement, cracks began to appear in the specimen, and the crack generation speed was accelerating. Then the change curve of crack number entered the high-speed propagation stage, in which the crack number of the sample increased the fastest. In contrast, the growth rate of shear stress decreased sharply until it reaches zero, and then the shear stress reached the peak state. Then, the shear stress curve decreased continuously, and the decreasing speed increases with the increase of JRC. Finally, the change curve of crack number entered the low-speed propagation stage, and the shear stress curve also entered the residual stage one after another.

For rough joints, there were obvious inflection points between the change curve of crack number and the shear stress curve, but not for smooth joints. On the whole, the shear stress will decrease after the failure of the sample, this indicates the crack development in the specimen can inhibit the growth of shear stress. When the shear stress rose rapidly, the crack in the sample had not developed obviously. When the growth rate of shear stress decreased rapidly, the number of cracks increased rapidly. This showed that the failure of the specimen had an obvious lag effect compared with the change of shear stress.

5. Distribution Law Of Average Stress In Joint Segment

In Section 3.1, we propose the progressive failure mechanism of joint samples in the shear process. However, there were no quantitative results to evaluate the contribution of different joint protrusions to resist shear stress. With the help of the measuring circle function embedded in PFC^{2D}, we had monitored the variation law of the mechanical indexes of the joint segment during the shear process.

5.1 Layout of measuring circle

The measuring circle cannot move after being arranged, and the horizontal and normal displacement will occur in the shear process of the upper test. This makes it impossible for the measuring circle to approximately monitor the data in the same area. Therefore, in this section, the layout of the measuring circle on the joint specimen is based on the fixed lower sample, and the monitoring scheme is shown in Fig. 14 (taking joint 10 as an example). Among them, the joint profile was divided into 10 segments, which were numbered from segment 1 to segment 10. A measuring circle was set on each joint segment. The center of the measuring circle was located on the joint profile, and the diameter was 10mm.

5.2 Average stress variation curve of different joint segments

By measuring circle function, we can measure the data of porosity, stress, strain rate, particle size distribution and coordination number in a specific area. In this section, the stress monitoring results are selected for corresponding analysis. As a variable in the continuous medium model, the stress can be approximately obtained only by averaging in the discrete medium³⁷. The specific calculation formula is as follows:

$$\bar{\sigma} = -\frac{1}{V} \times \sum_0^{N_c} F^{(c)} \otimes L^{(c)} \quad (9)$$

Where, V is the volume of the measuring circle, which is the area in the two-dimensional model; N_c is the number of active contacts in the measurement circle; $F^{(c)}$ is the vector for measuring the contact force in the circle; $L^{(c)}$ is the branch vector connecting the centroids of two particles; represents the vector product³⁷. According to the direction, the average stress monitored by the measuring circle is mainly divided into horizontal stress (stress xx), vertical stress (stress yy) and tangential stress (stress xy or stress yx). The first two were selected for representative description in this paper. After preliminary calculation, we found that the average stresses in the horizontal and vertical directions monitored by the measuring circle under all schemes are compressive stresses. Therefore, the subsequent analysis would no longer distinguish the stress attribute, but only analyze the stress value.

Figure 15 shows the variation curve of horizontal and vertical stress for different joint segments under 2MPa normal stress. The figure on the left shows the horizontal stress and the figure on the right shows the vertical stress. The 1th, 4th, 7th and 10th joints specimens were selected for representative description.

It could be seen that the horizontal stress of each joint section was small at the beginning of shear process, and the value of vertical stress was kept around 2MPa, which was basically consistent with the external normal stress. During the shear process, the horizontal stress of each joint segment gradually increased, then decreased, and finally remained stable. In addition, the stress in different joint segment was different, and the rougher the joint was, the more obvious the difference was. Taking the 10th joint as an example, the horizontal stress of the 3th joint segment was much greater than that of another joint segment. Combined with the geometric morphology of the joint, the 3th joint segment corresponded to the position of maximum protrusion. It could be verified that there was a strong correlation between the stress distribution of each joint segment and its surface morphology.

With the increase of shear displacement, the vertical stress at some joint segments gradually decreased to 0 MPa as a whole. This indicated that these joint segments were no longer in contact. As the external normal stress was always constant in the shear process, the joint segments bearing the external normal stress were significantly reduced. On the right side of Fig. 15, we could see that the vertical stress at some joint sections had increased significantly, which indicated that there was stress concentration here. Besides, the shear displacement nodes corresponding to the significant increase of vertical stress in the joint section were different. This showed that the position of the joint segment mainly bearing the normal stress would change during the shear process.

5.3 Distribution law of maximum stress in different joint segment

As an important index to evaluate the mechanical properties of joint surface, shear strength is most widely used in practical engineering. In order to discuss the contribution of different protrusions to the overall roughness of the joint surface, the distribution law of the maximum stress of each protrusion in the pre peak stage of shear stress are further analyzed in this section.

Based on the test data in section 4.1, the shear displacement range corresponding to the pre peak stage of the shear stress curve of each scheme was firstly obtained. Then, the maximum value of stress curve in the corresponding shear displacement range was obtained, and the results are shown in Fig. 16. Where, Fig. 16(a) to (e) are the analysis results of the 6th to 10th joint specimens respectively. The left side is horizontal stress and the right side is vertical stress. Each figure contains four cases of different normal stresses.

As shown in Fig. 16, the distribution law of the maximum horizontal stress and the maximum vertical stress of the joint segment under each scheme was very similar, especially the 6th, 8th and 10th joint specimens. With the increase of normal stress, the stress in the joint section increased, but the overall distribution law was basically unchanged. This shows that the proportion of shear force shared by different joint segments was basically constant when the joint segments are subjected to the dual action of shear stress and normal stress.

In addition, the maximum values of horizontal and vertical stresses that different joint segments bear in the pre peak stage of shear stress are different. For the 8th joint, the maximum horizontal and vertical

stresses at the joint segment 5 were greater than those in other joint segments. By comparing the geometric profile of the 8th joint in Fig. 3, it could be seen that the joint segment 5 coincided with the position of largest protrusion of the joint surface. For the 10th joint, the maximum horizontal and vertical stresses of joint segment 3 were also greater than those of other joint segments, and the joint segment 3 was also at the largest protrusion of the joint surface. In short, the stress bearing capacity of joint segments at different positions on the joint surface was closely related to the morphological characteristics of the joint itself. This was consistent with the results shown in the macro failure diagram of joint specimen in section 4.2.

5.4 Relationship between JRC and upper limit of maximum stress in different joint segment

In order to further reveal the relationship between the joint roughness and the stress of the joint segment, the upper limit of the maximum stress of the joint segment under each scheme were calculated in this section, as shown in Fig. 17. Where, the left side is the case of horizontal stress and the right side is the case of vertical stress.

It could be seen that, with the increase of joint JRC, the upper limit of the maximum horizontal stress in the joint segment kept increasing as a whole. This meant that the ability of the joint segment to bear horizontal stress were becoming stronger as the JRC increased. However, the joint JRC had no regular effect on the upper limit of the maximum vertical stress of the joint section. In addition, with the increase of the external normal stress, the upper limit of the maximum horizontal stress and the maximum vertical stress of the joint segment increased as a whole. Moreover, the regularity of the former was obviously better than that of the latter.

5.5 Relationship between JRC and distribution range of maximum stress in different joint segments

In order to analyze the distribution characteristics of stress bearing capacity of joint segments, the upper limit of the maximum stress of the joint segment under each scheme were calculated in this section, as shown in Fig. 18. Where, the left side is the case of horizontal stress and the right side is the case of vertical stress.

It could be seen that with the increase of joint JRC, the distribution range of the maximum horizontal stress in each joint section showed an increasing trend, but there was no obvious law in the distribution range of the maximum vertical stress. In addition, with the increase of normal stress from 2MPa to 8MPa, the range of the maximum value of horizontal stress and vertical stress in each joint section had been significantly expanded as a whole. Similarly, the distribution range of the maximum horizontal stress was more affected by JRC and normal stress than that of vertical stress.

Conclusion

In order to reveal the local shear failure mechanism of rough joints during the shear process, the numerical direct shear tests of Barton's 10 typical joints under different normal stresses were carried out

using PFC^{2D} in the DEM. The MSJM was introduced to simulate the mechanical properties of joints, and the servo mechanism was set to keep the normal stress constant. According to the test results, the variation of shear stress, overall failure law and local shear mechanism of rough joints were discussed in detail. The results showed that there were strong differences in the shear stresses borne by the local segments of rough joints and it was closely related to the geometric morphology of the joint segments. The main conclusions are as follows:

Barton's 10 typical joints were digitized by image processing software and the accuracy of the data is verified by the correlation between the statistical parameters (Z_2 and R_p-1) and JRC. In the direct shear test of joint samples implemented by PFC^{2D}, the microscopic parameters of intact rock and joint were calibrated by comparing numerical test with physical test and the normal stress was constantly applied through the servo mechanism. This showed that the research results of this paper are reliable.

With the increase of JRC and normal stress, the shear stress and shear strength of joints showed an obvious increasing trend. This law was consistent with physical experiments. During the shearing process, the specimen failure and contact force mainly started and concentrated at the largest protrusion, and gradually turned to other protrusions positions in the later stage of shear process. With the increase of shear displacement, the change of shear stress had a good corresponding relationship with the failure speed of the sample. Crack propagation can significantly inhibit the growth of shear stress, which made the change of crack number lag behind the shear stress as a whole.

Based on the measuring circle function, the variation law of average stress in different 10 joint segments during shear process were tracked. The 3 stress indexes including maximum stress, upper limit of maximum stress and distribution range of maximum stress were selected to describe the contribution of local joint segments in resisting shear stress. The above 3 stress indexes were confirmed to have a good regularity with JRC of joint. Among them, as the JRC increased, the stress parameters in the horizontal direction increased. For local joint segments, the external shear stress bore a good corresponding relationship with its protrusion size, which well verified the difference in the contribution of joint geometry to the overall roughness.

In this paper, the local shear mechanism of joint segments was qualitatively and quantitatively presented separately and verified to be completely different. In the subsequent studies, the different contributions of joint segments are suggested to be noticed according to their protrusion size.

Declarations

Data Availability

The data used to support the findings of this study are included within the article.

Acknowledgments

This study was funded by the National Natural Science Foundation of China (11902249, 51179153, 11872301), Natural Science Basic Research Program of Shaanxi (2020JM-453), and Scientific Research Program of Shaanxi Provincial Education Department (17JS091, 2019JQ-395). Their support is gratefully acknowledged.

Author contributions

J.Y.H. designed the study and wrote the main manuscript text, Z.Q.Z. did most of the work of joint profile data acquisition and verification, J.Y.H. and M.M.H. conducted most numerical direct shear tests of joint specimens, N.L. prepared figures and tables. M.D.H. checked the language. All authors reviewed the manuscript.

Conflicts of Interest

The authors declare that they have no conflicts of interest.

References

1. Allegre C.J., Mouel J. & Provost A. Scaling rules in rock fracture and possible implications for earthquake prediction. *Nature***297**, 47-49 (1982).
2. He M., Zhang Z., Zhu J. & Li N. Correlation between the constant m of Hoek-Brown criterion and porosity of intact rock. *Rock Mechanics and Rock Engineering*. Online Published November (2021).
3. Pollard D. D. & Segall P. Theoretical displacements and stresses near fractures in rock: with applications to faults, joints, veins, dikes, and solution surfaces. *Fracture Mechanics of Rock***13**, 277-349 (1987).
4. Huan J., He M., Zhang Z. & Li N. Parametric study of integrity on the mechanical properties of transversely isotropic rock mass using DEM. *Bulletin of Engineering Geology and the Environment***79**, 2005-2020 (2020).
5. Hoek E. Strength of jointed rock masses. *Géotechnique***33**, 187-223 (1983).
6. He M. et al. Correlation between the rockburst proneness and friction characteristics of rock materials and a new method for rockburst proneness prediction: Field demonstration. *Journal of Petroleum Science and Engineering***205**, 108997 (2021).
7. Yang B., He M., Zhang Z., Zhu J. & Chen Y. A New Criterion of Strain Rockburst in Consideration of the Plastic Zone of Tunnel Surrounding Rock. *Rock Mechanics and Rock Engineering*, 1-13 (2022).
8. Yang X., Kulatilake P. H. S. W., Jing H. & Yang S. Numerical simulation of a jointed rock block mechanical behavior adjacent to an underground excavation and comparison with physical model test results. *Tunnelling & Underground Space Technology***50**, 129-142 (2015).
9. Patton F. D. Multiple modes of shear failure in rock. *Proceeding of the Congress of International Society of Rock Mechanics*, 509-513 (1966).

10. Li Y., Oh J., Mitra R. & Hebblewhite B. A constitutive model for a laboratory rock joint with multi-scale asperity degradation. *Computers and Geotechnics***72**, 143-151 (2016).
11. Tang Z. et al. Mechanical model for predicting closure behavior of rock joints under normal stress. *Rock Mechanics & Rock Engineering***47**, 2287-2298 (2014).
12. Wang J., Mao L., Yang Y. & Cao Q. Behavior of microcontacts in rock joints under direct shear creep loading. *International Journal of Rock Mechanics and Mining Sciences* **78**, 217-229 (2015).
13. Lee H. S., Park Y. J., Cho T. F. & You K. H. Influence of asperity degradation on the mechanical behavior of rough rock joints under cyclic shear loading. *International Journal of Rock Mechanics & Mining Sciences***38**, 967-980 (2001).
14. Li Y., Oh J., Mitra R. & Hebblewhite B. Experimental Studies on the Mechanical Behaviour of Rock Joints with Various Openings. *Rock Mechanics and Rock Engineering***49**, 837-853 (2016).
15. Jiang Y., Li B. & Tanabashi Y. Estimating the relation between surface roughness and mechanical properties of rock joints. *International Journal of Rock Mechanics and Mining Sciences***43**, 837-846 (2006).
16. Hong E. S., Lee I. M., Cho G. C. & Lee S.W. New approach to quantifying rock joint roughness based on roughness mobilization characteristics. *KSCCE Journal of Civil Engineering***18**, 984-991 (2014).
17. Indraratna B., Premadasa W., Brown E. T., Gens A. & Heitor A. Shear strength of rock joints influenced by compacted infill. *International Journal of Rock Mechanics and Mining Sciences***70**, 296-307 (2014).
18. Kumar R. & Verma A. K. Anisotropic shear behavior of rock joint replicas. *International Journal of Rock Mechanics and Mining Sciences***90**, 62-73 (2016).
19. Liu X. G., Zhu W. C., Yu Q. L. Chen S.J. & Li R. F. Estimation of the joint roughness coefficient of rock joints by consideration of two-order asperity and its application in double-joint shear tests. *Engineering Geology***220**, 243-255 (2017).
20. Wang S. Y., Sloan S. W., Tang C. A. & Zhu W. C. Numerical simulation of the failure mechanism of circular tunnels in transversely isotropic rock masses. *Tunnelling and Underground Space Technology***32**, 231-244 (2012).
21. Dan D. Q. & Konietzky H. Numerical simulations and interpretations of Brazilian tensile tests on transversely isotropic rocks. *International Journal of Rock Mechanics & Mining Sciences***71**, 53-63, (2014).
22. Potyondy D. O. The bonded-particle model as a tool for rock mechanics research and application: current trends and future directions. *Geosystem Engineering***18**, 1-28 (2015).
23. Cho N. Discrete element modeling of rock pre-peak fracturing and dilation. *University of Alberta(phd)*, (2008).
24. Xia L. & Zeng Y. Parametric study of smooth joint parameters on the mechanical behavior of transversely isotropic rocks and research on calibration method. *Computers and Geotechnics***98**, 1-7 (2018).

25. Bahaaddini M., Hagan P. C., Mitra R. & Hebblewhite B. K. Scale effect on the shear behaviour of rock joints based on a numerical study. *Engineering Geology***181**, 212-223 (2014).
26. Bahaaddini M., Sharrock G. & Hebblewhite B. K. Numerical direct shear tests to model the shear behaviour of rock joints. *Computers and Geotechnics***51**, 101-115 (2013).
27. Tan X., Konietzky H., Frühwirt T. & Dan D.Q. Brazilian tests on transversely isotropic rocks: laboratory testing and numerical simulations. *Rock Mechanics & Rock Engineering***48**, 1341-1351 (2015).
28. Debecker B. & Vervoort A. Two-dimensional discrete element simulations of the fracture behaviour of slate. *International Journal of Rock Mechanics and Mining Sciences***61**, 161-170 (2013).
29. Yang Z. Y., Lo S. C. & Di C. C. Reassessing the Joint Roughness Coefficient (JRC) Estimation Using Z2. *Rock Mechanics & Rock Engineering***34**, 243-251 (2001).
30. Yu X. & Vayssade B. Joint profiles and their roughness parameters. *International Journal of Rock Mechanics & Mining Sciences & Geomechanics Abstracts***28**, 333-336, (1991).
31. Barton N. Review of a new shear-strength criterion for rock joints. *Engineering Geology***7**, 287-332, (1973).
32. Barton N. & Choubey V. The shear strength of rock joints in theory and practice. *Rock Mechanics***10**, 1-54, (1977).
33. International Society of Rock Mechanics, Suggested methods for the quantitative description of discontinuities in rock masses. *International Journal of Rock Mechanics & Mining Science and Geomechanics Abstracts***15**, 319-368, (1978).
34. Tatone B. S. A. & Grasselli G. A new 2D discontinuity roughness parameter and its correlation with JRC. *International Journal of Rock Mechanics and Mining Sciences***47**, 1391-1400 (2010).
35. Jang H. S., Kang S. S. & Jang B. A. Determination of Joint Roughness Coefficients Using Roughness Parameters. *Rock Mechanics & Rock Engineering***47**, 2061-2073 (2014).
36. Huan J. Y., He M. M., Zhang Z. Q. & Li N. A New Method to Estimate the Joint Roughness Coefficient by Back Calculation of Shear Strength. *Advances in Civil Engineering***2019**, 1-15 (2019).
37. Itasca Consulting Group Inc. *PFC2D manual, version 5.0 Minneapolis, Minnesota*, (2014).

Figures

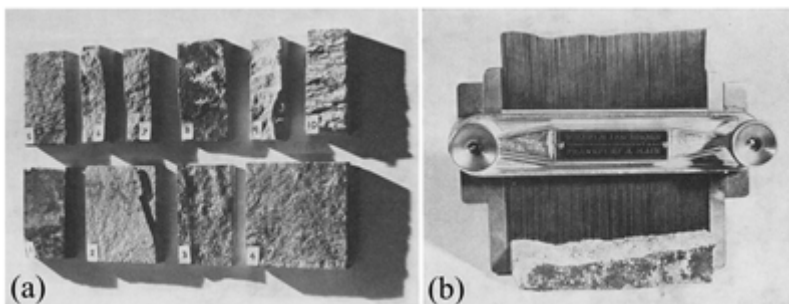


Figure 1

Method of using a comb to get roughness profile from joint surface^{31,32}. (a) 10 typical joint surfaces; (b) profile comb.

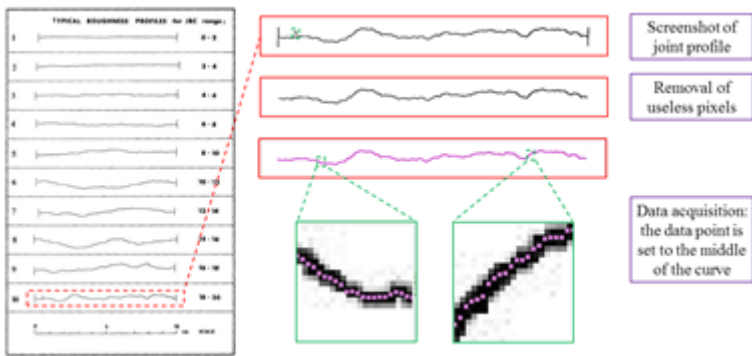


Figure 2

The diagram used to show digitization of a joint profile.

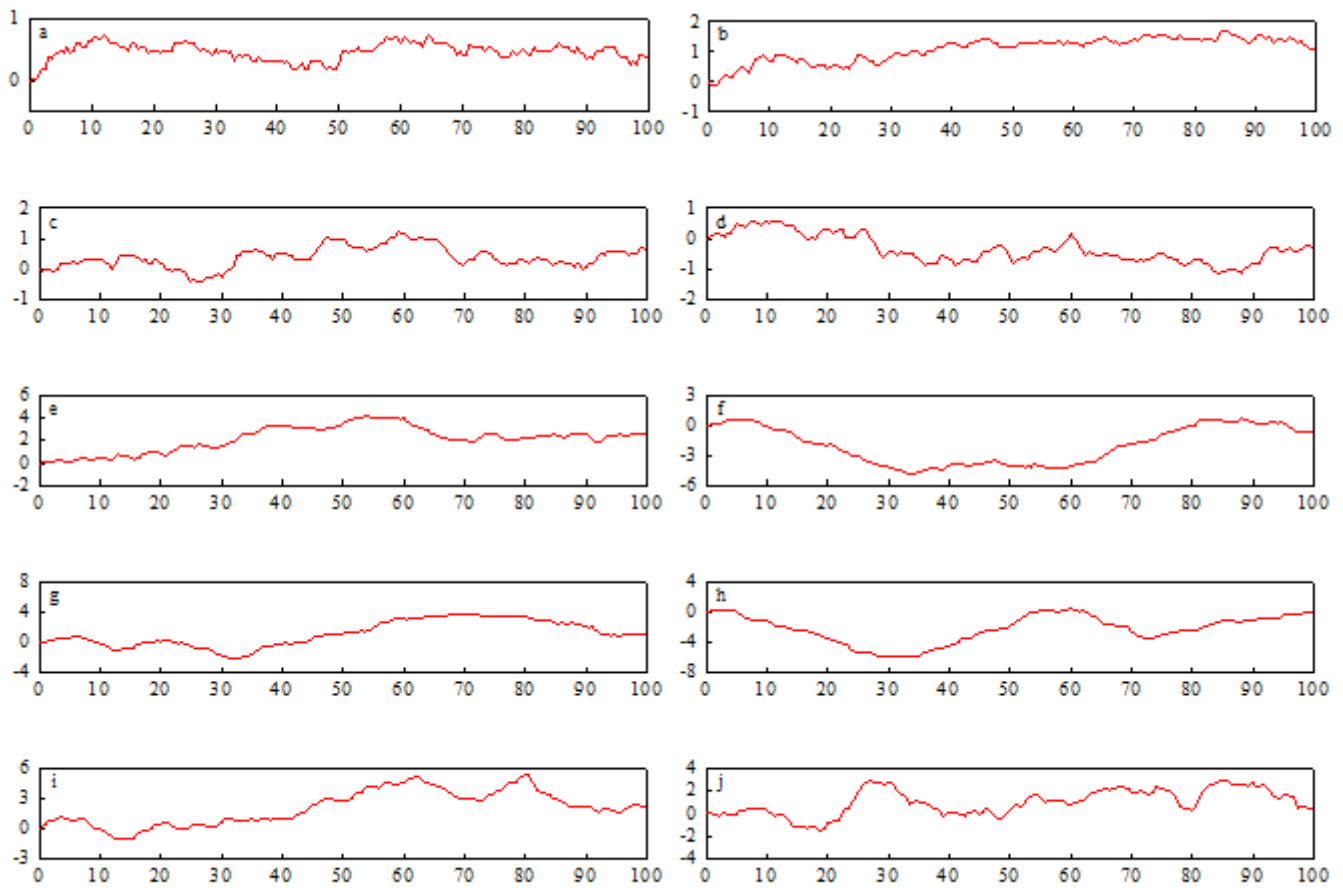


Figure 3

The modified 10 standard roughness joint profiles (Unit: mm). (a) Profile 1; (b) Profile 2; (c) Profile 3; (d) Profile 4; (e) Profile 5; (f) Profile 6; (g) Profile 7; (h) Profile 8; (i) Profile 9; (j) Profile 10.

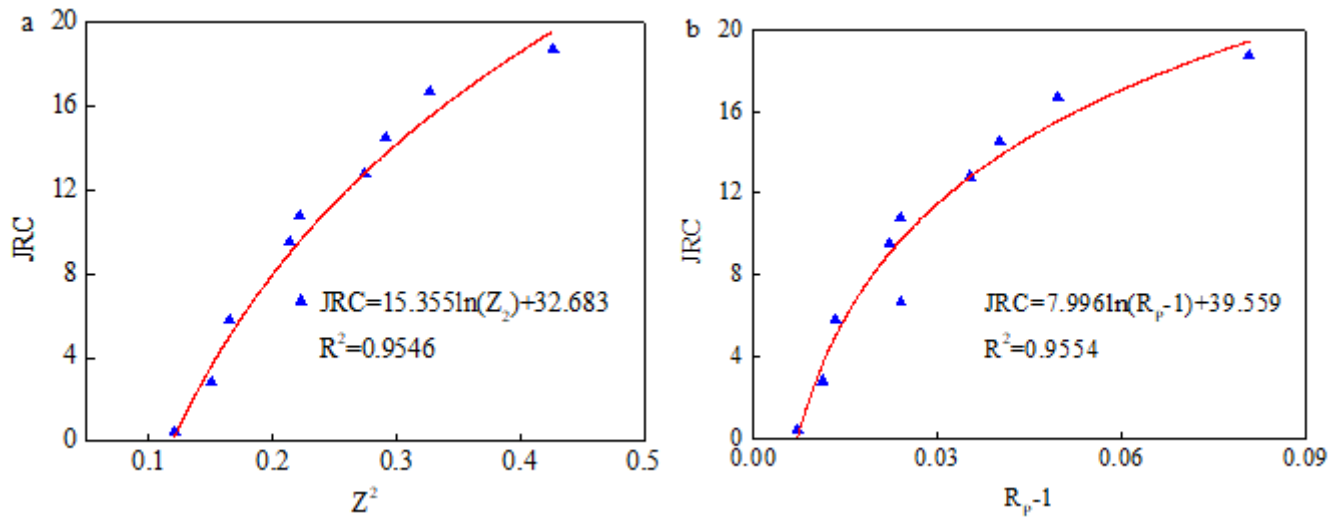


Figure 4

Fitting curves between statistical parameters and JRC. (a) Z^2 ; (b) $R_p - 1$.

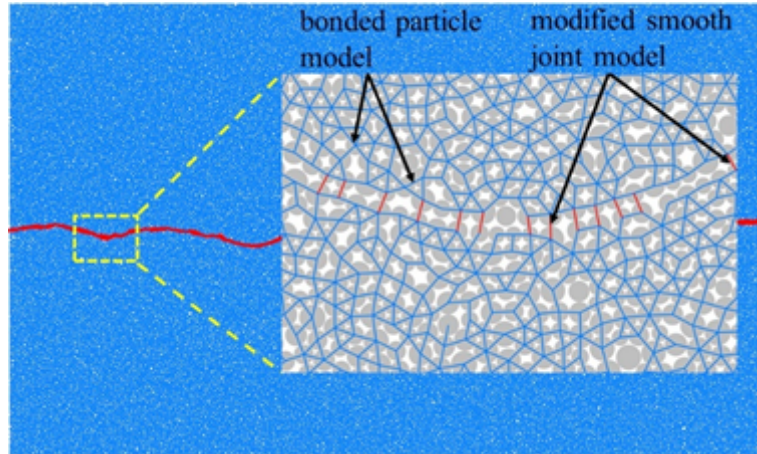


Figure 5

Numerical joint model established by the smooth joint model.

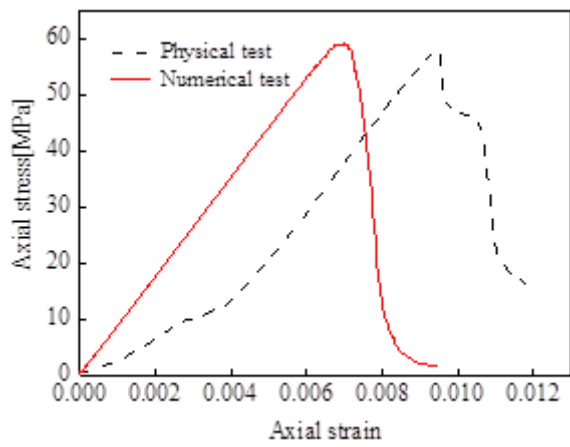


Figure 6

Results of uniaxial compression tests of intact rock.

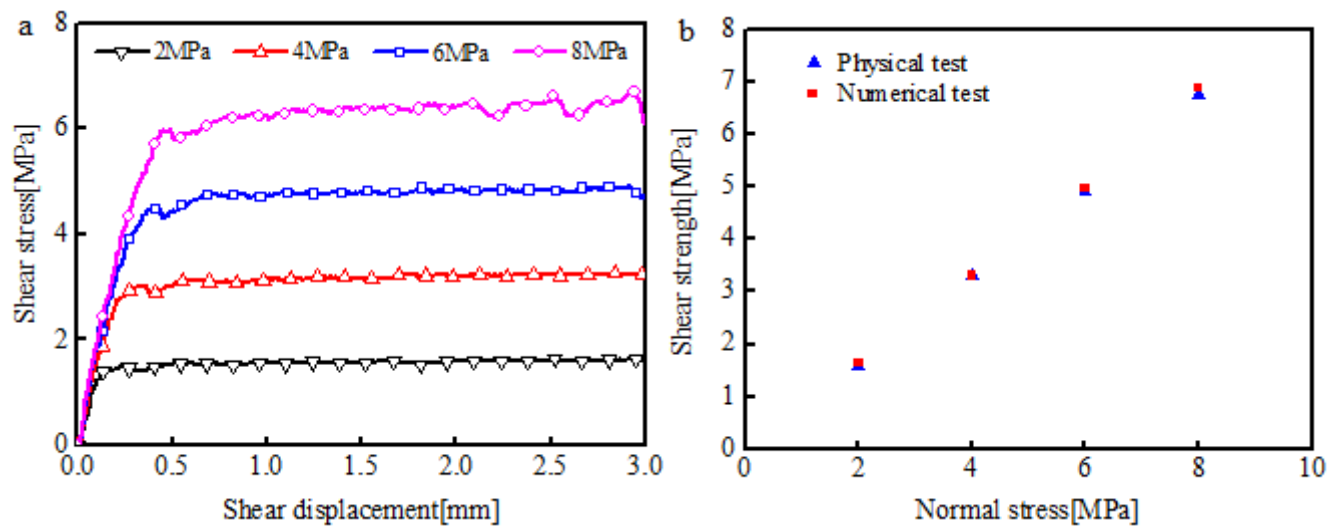


Figure 7

Numerical direct shear test results of plane joints.

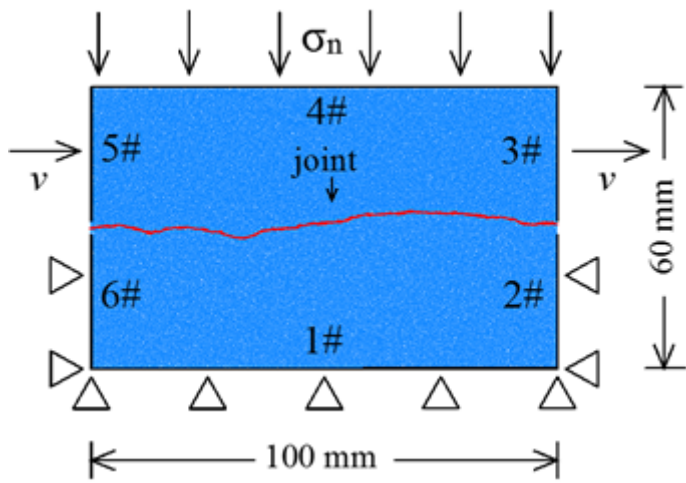


Figure 8

The scheme of numerical direct shear test.

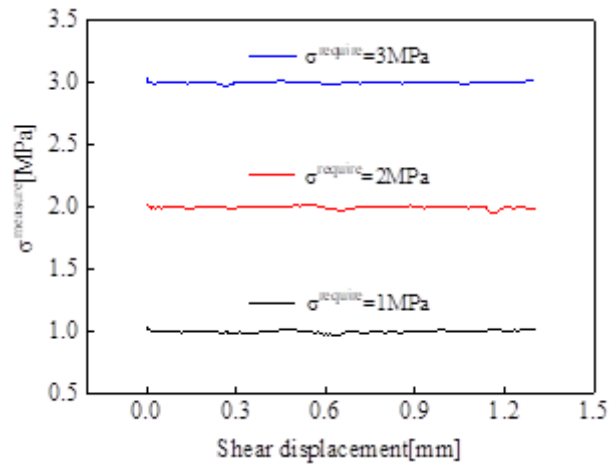


Figure 9

Comparison between actual normal stress and expected normal stress.

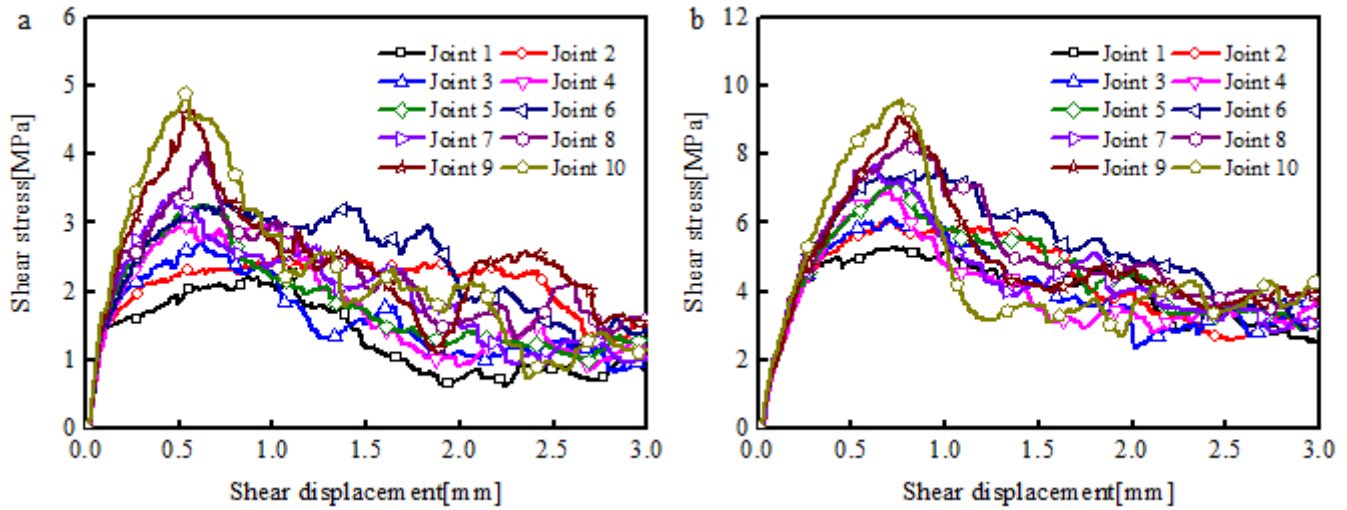


Figure 10

Shear stresses-shear displacement curves of joint specimens with different roughness. (a) 2MPa (b) 6MPa.

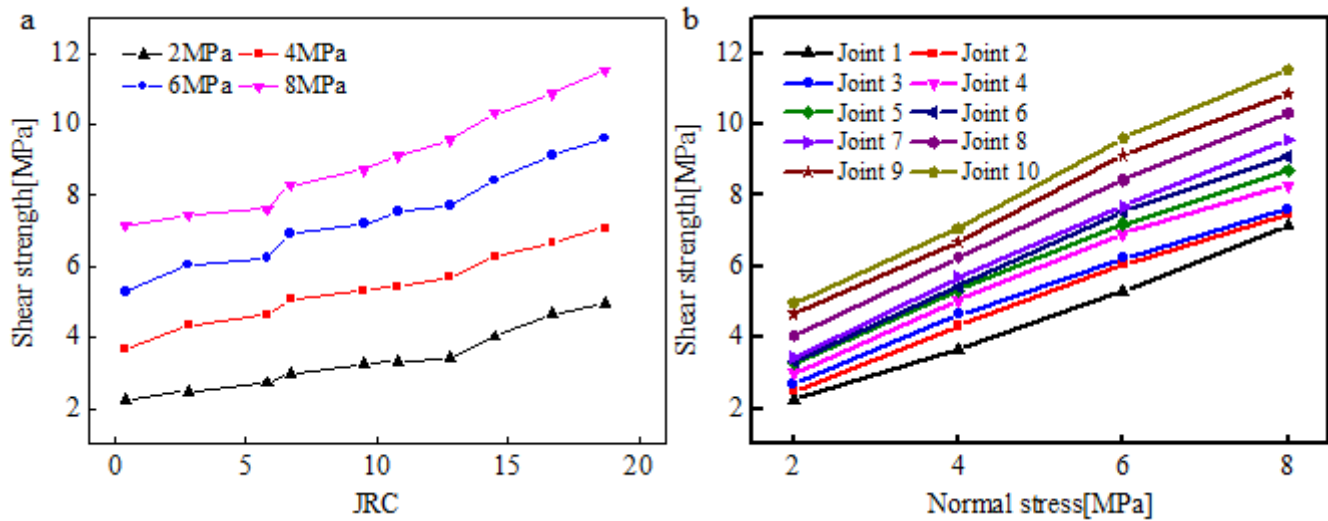


Figure 11

The influence of JRC and normal stress on the shear strength of joint specimens. (a) the influence of JRC; (b) the influence of normal stress.

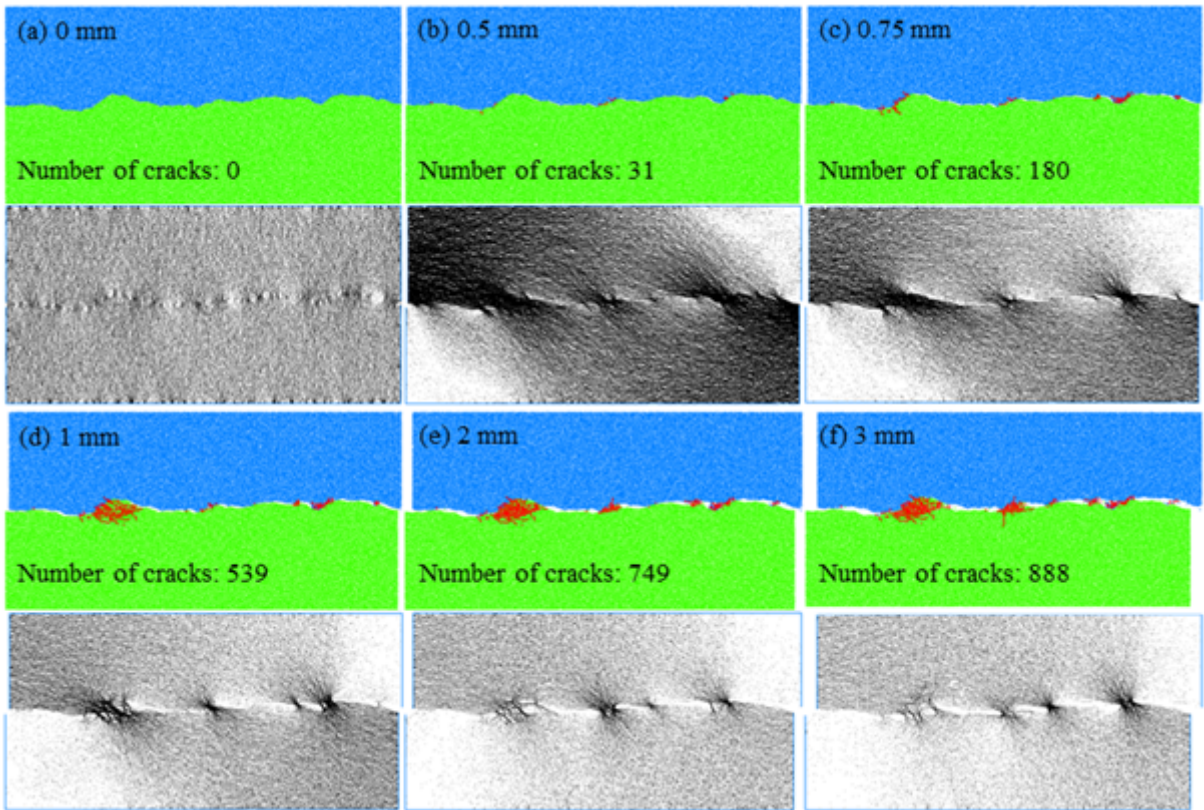


Figure 12

Contrast diagram of crack propagation and contact force distribution of joint specimen during shear process. (a) 0mm; (b) 0.5mm; (c) 0.75mm; (d) 1mm; (e) 2mm; (f) 3mm.

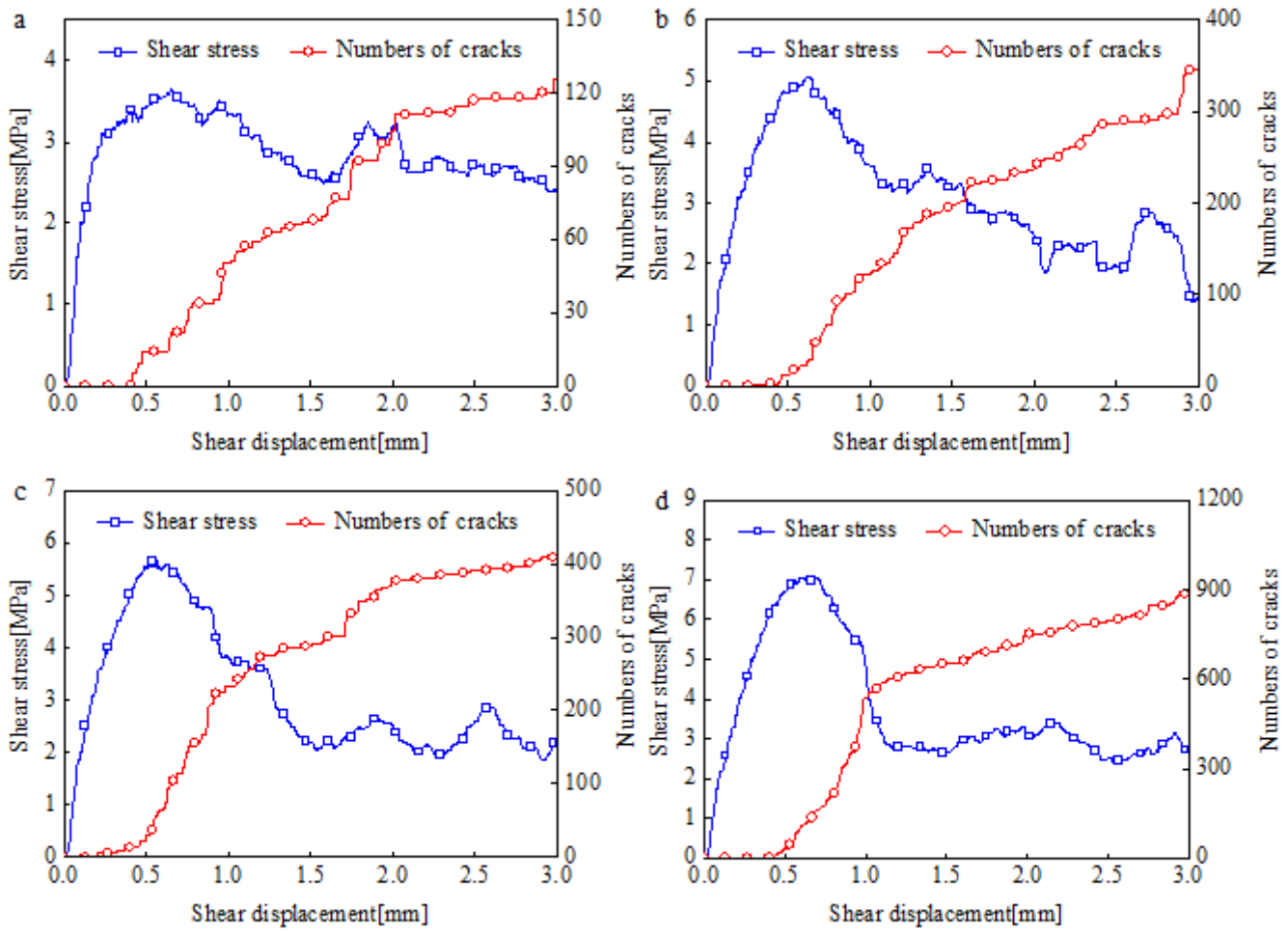


Figure 13

Change curves of shear stress and crack number with shear displacement. (a) the 1th joint; (b) the 4th joint; (c) the 7th joint; (d) the 10th joint.

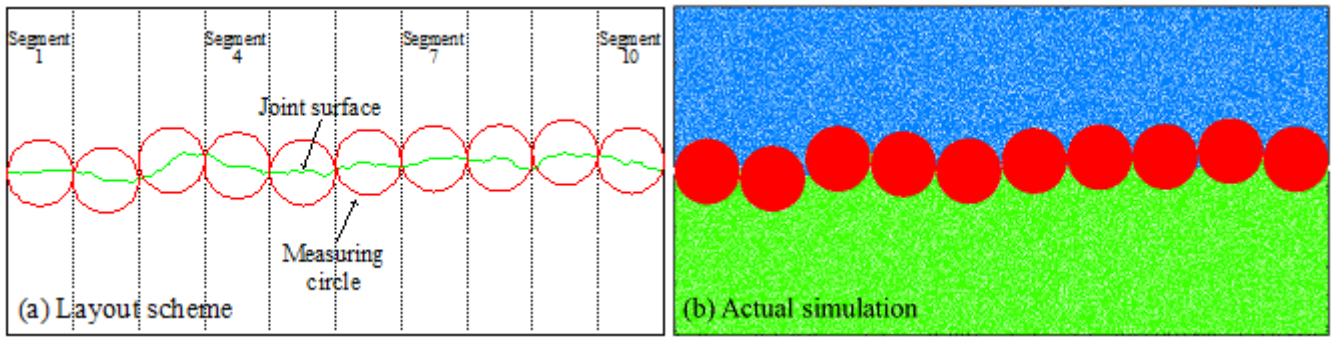


Figure 14

Layout of measuring circles. (a) layout scheme; (b) actual simulation.

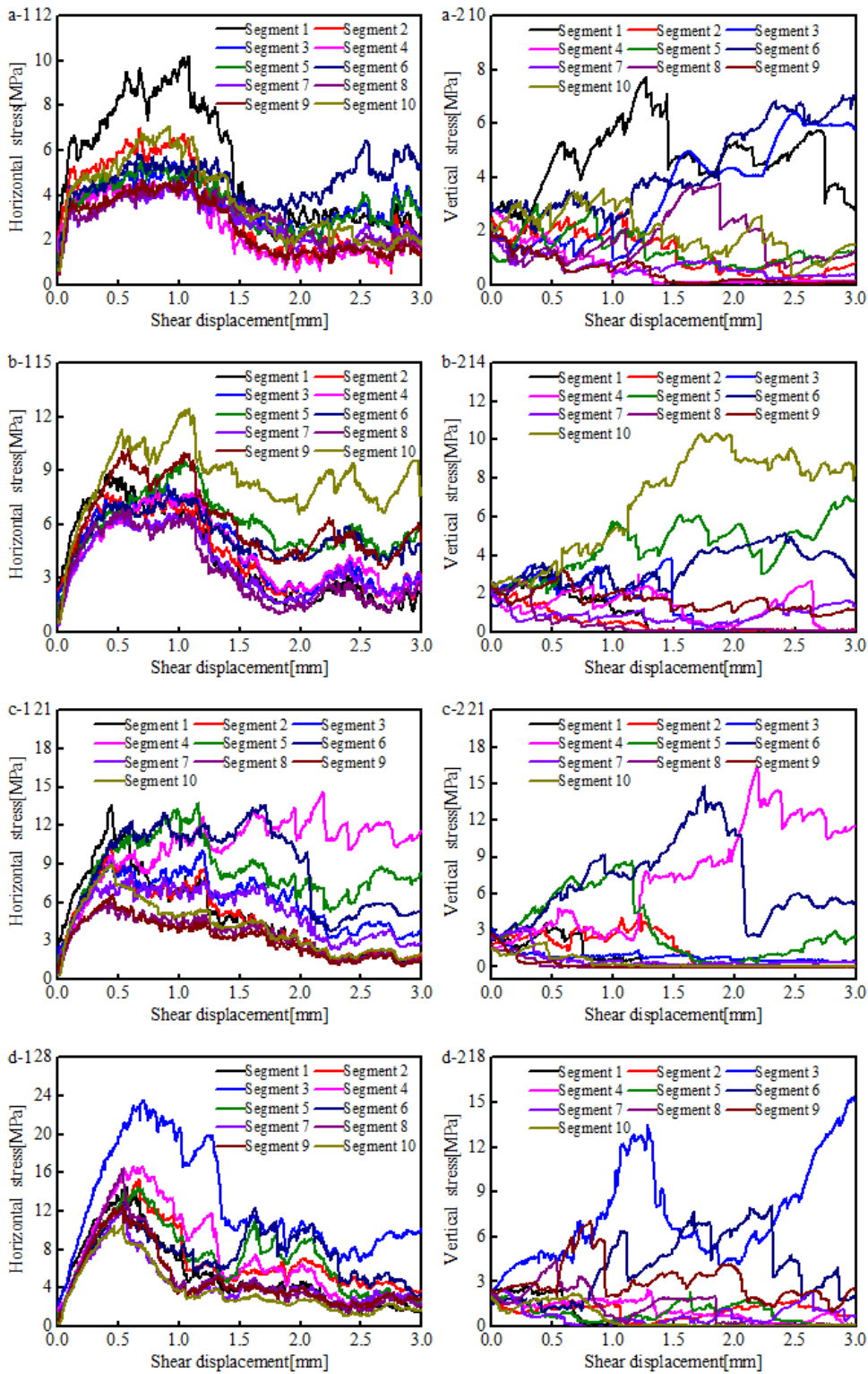


Figure 15

Change curves of horizontal and vertical stress of different joint segments during shear process. (a) the 1th joint; (b) the 4th joint; (c) the 7th joint; (d) the 10th joint.

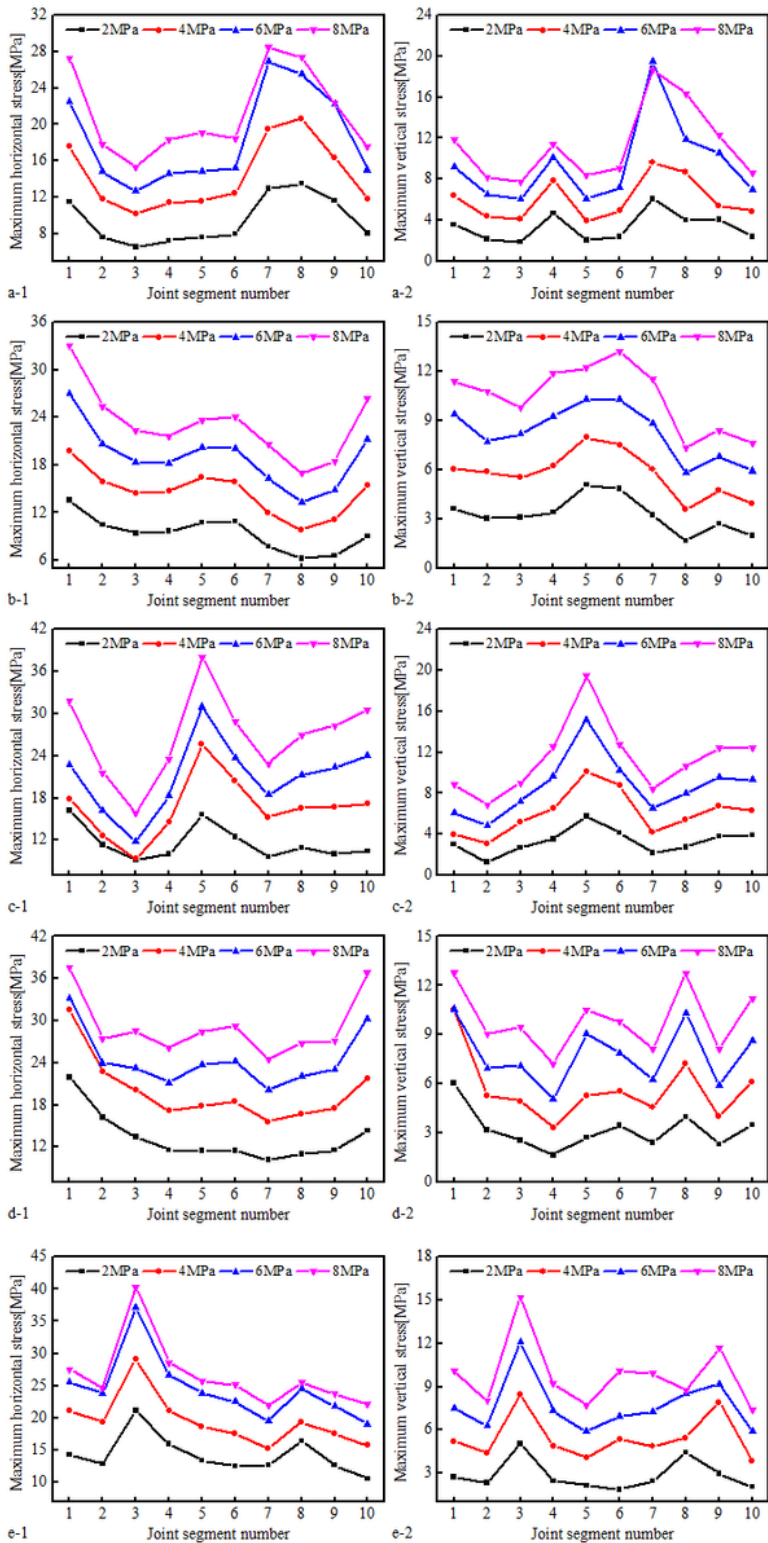


Figure 16

Maximum stress distribution of joint segments under different normal stresses. (a) the 6th joint; (b) the 7th joint; (c) the 8th joint; (d) the 9th joint; (e) the 10th joint.

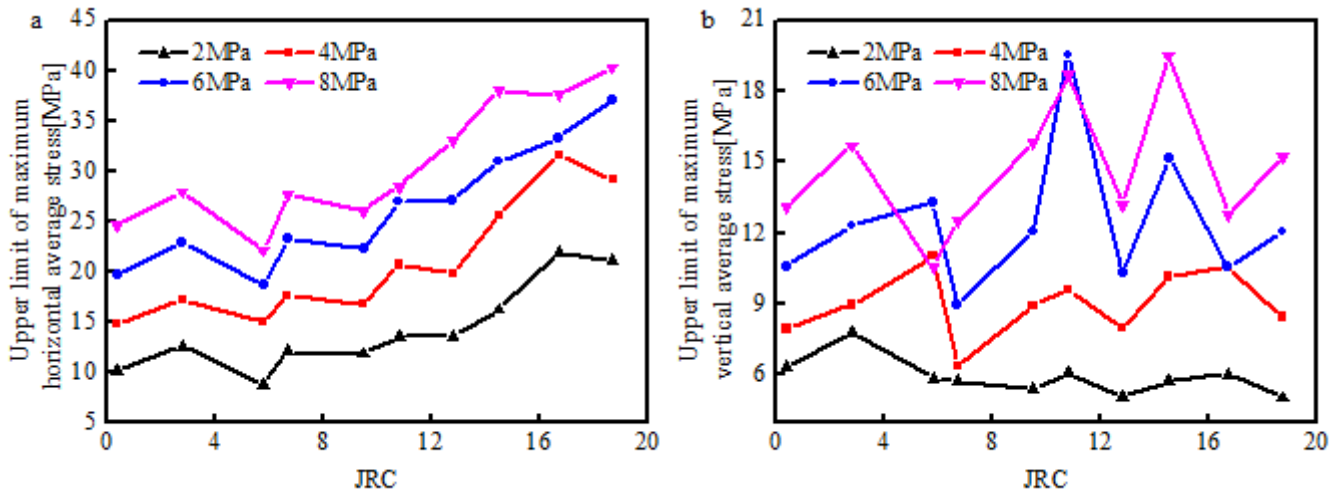


Figure 17

Influence of joint JRC on the upper limit of maximum stress of joint segments. (a) Horizontal stress; (b) Vertical stress.

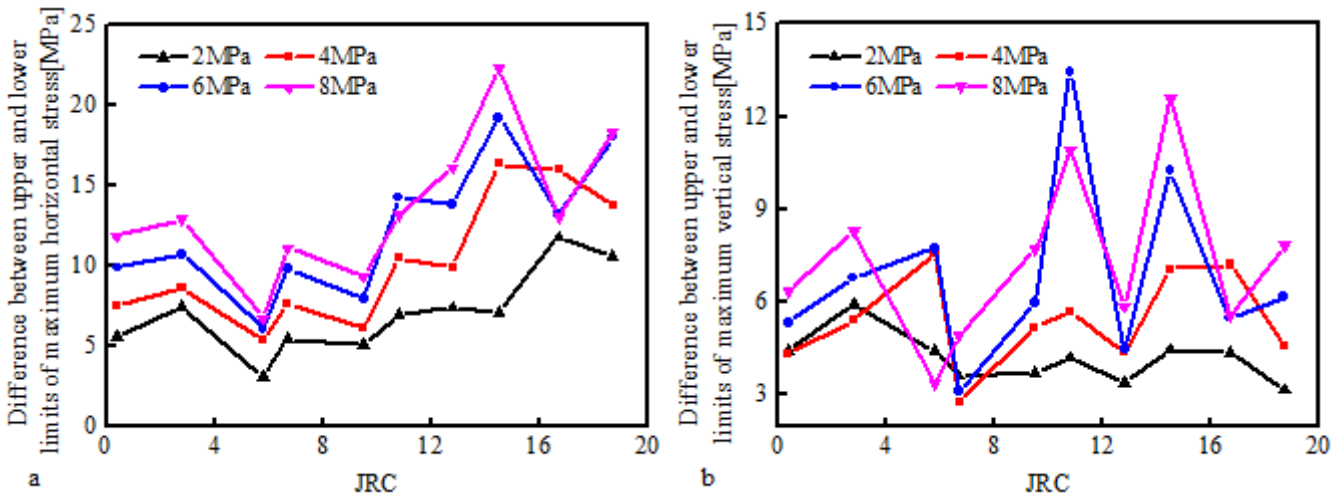


Figure 18

Influence of joint JRC on the distribution range of maximum stress of joint segments. (a) the horizontal stress; (b) the vertical stress.